

## Aggregation in Dilute Solutions of 1-Hexanol in *n*-Hexane: A Monte Carlo Simulation Study

John M. Stubbs and J. Ilja Siepmann\*

Departments of Chemistry and of Chemical Engineering and Materials Science, University of Minnesota, 207 Pleasant Street SE, Minneapolis, Minnesota 55455-0431

Received: October 10, 2001

Configurational-bias Monte Carlo simulations in the isobaric–isothermal ensemble using the nonpolarizable TraPPE–UA (transferable potentials for phase equilibria–united-atom) force field were performed to study the aggregation of 1-hexanol in *n*-hexane. The spatial distribution of alcohols was sampled efficiently using special Monte Carlo moves. Analysis of the microscopic structures for 1, 3, and 5% solutions at a temperature of 298.15 K and a pressure of 101.3 kPa shows strong aggregation with a preference for tetramers and pentamers for all three concentrations. About half of these tetramers and pentamers are found in cyclic aggregates. The enthalpies for the formation of clusters of specific sizes were determined from simulations of a 3% solution at temperatures ranging from 298.15 to 328.15 K. The free energies and enthalpies of cluster formation show the large influences of hydrogen-bond cooperativity, which favors clusters larger than dimers, but a decreasing enthalpy gain and an increasing entropic penalty prevent the formation of very large clusters. These results have important implications for the thermodynamic modeling of hydrogen-bonding fluids, which commonly use a constant value for the free energy of hydrogen-bond formation. Overall agreement with Fourier transform infrared spectroscopic measurements on the extent of hydrogen bonding for the same mixtures is satisfactory.

### 1. Introduction

The formation of hydrogen bonds plays a dominant role in many chemical and biological processes.<sup>1,2</sup> The hydrogen bond is special because its strength and directionality lie between those of weak *chemical* bonds and strong *physical* intermolecular interactions.<sup>3</sup> The ability to form hydrogen bonds between a hydrogen donor site and a lone-pair acceptor site usually leads to association, and the prediction of solution behavior for mixtures involving hydrogen-bonding components is a challenge. Although many thermodynamic models employ a chemical description of the hydrogen bond,<sup>1,4</sup> it is usually described in terms of the Coulombic interaction of partial charges in molecular simulation studies.<sup>5</sup> It is well-known that cooperativity plays an important role in the formation of hydrogen-bonded aggregates, i.e., the strength of a newly formed hydrogen bond can be enhanced by the presence of already-formed hydrogen bonds as the electronic charge distribution responds to the polar environment.<sup>6–8</sup> However, most thermodynamic models use a common equilibrium constant for the addition of a molecule to a hydrogen-bonded cluster, irrespective of whether it involves the formation of a dimer or of a larger aggregate. Similarly, the commonly used nonpolarizable force fields neglect any changes of the electronic structure but include some cooperativity due to favorable dipole–dipole interactions of molecules that are not directly hydrogen-bonded.

Recently, Gupta and Brinkley<sup>9</sup> used Fourier transform infrared (FTIR) spectroscopy to measure the extent of aggregate formation in dilute solutions of 1-hexanol or 1-pentanol dissolved in *n*-hexane. In addition, Sum and Sandler<sup>10</sup> used ab initio calculations to investigate the energetics of clusters of methanol (up to hexamers), ethanol, or 1-propanol (up to tetramers). The two studies both point to the importance of hydrogen-bond cooperativity, but they reach different conclusions on the cluster

size dependence of the hydrogen-bond cooperativity. Although the concentration of free hydrogen-bond donors can be determined directly using FTIR spectroscopy from the area of the free O–H stretching peak (at about 3650 cm<sup>−1</sup>), it is not possible to resolve the broad bonded O–H peak (in the range of 3200–3600 cm<sup>−1</sup>) according to specific aggregate sizes.<sup>9</sup> Gupta and Brinkley showed that the experimental results for the percentage of free O–H bonds cannot be described satisfactorily by theoretical models that neglect hydrogen-bond cooperativity and introduced a new model that utilizes two different hydrogen bonds: dimer-like and polymer-like. A dimer-like hydrogen bond is formed when a given alcohol molecule acts solely as hydrogen-bond donor but has a free acceptor site, whereas a polymer-like bond is formed when the donor alcohol molecule is also the acceptor of a previously formed hydrogen bond. In the derivation of their hydrogen-bond cooperativity model, Gupta and Brinkley<sup>9</sup> considered only the formation of linear aggregates, neglecting branched and cyclic aggregates. Nevertheless, using an equilibrium constant for the polymer-like hydrogen bond that is 10 times larger than that for the dimer-like hydrogen bond, the theory of Gupta and Brinkley yields excellent agreement with the experimentally measured extent of hydrogen bonding in the (1-hexanol or 1-pentanol)/*n*-hexane mixtures.

The ab initio calculations of Sum and Sandler provide clear evidence for hydrogen-bond cooperativity in alcohol clusters (shortening of the O–O distances, increases in the Mulliken charges, and increases in the binding energy).<sup>10</sup> Assuming that the change in entropy due to the addition of one molecule to a hydrogen-bonded chain (either linear or cyclic) is independent of the chain length, Sum and Sandler<sup>10</sup> found that the ratios of equilibrium constants for forming multimer hydrogen bonds to that for dimer formation increase rapidly from trimer to pentamer before leveling off. A more pronounced cooperativity effect was observed for cyclic clusters than for linear clusters.

\* Corresponding author. E-mail: siepmann@chem.umn.edu.

The goal of the present molecular simulation study is to complement the previous experimental, theoretical, and ab initio investigations on the extent of aggregate formation and hydrogen-bond cooperativity in alcohol/alkane mixtures. The main advantages of molecular simulations are that they allow us to gain direct microscopic insight into the distributions of aggregate sizes and structures (linear, cyclic, or branched) and that both enthalpic and entropic effects are allowed to play a role in the formation of hydrogen-bonded aggregates. The nonpolarizable, united-atom (UA) version of the transferable potential for phase equilibria (TraPPE) force field<sup>11,12</sup> was used in this study, because simulations of dilute mixtures require large system sizes and the use of polarizable, all-atom force fields would be too demanding for the present computational resources. The remainder of this paper is organized as follows. First, we briefly describe the molecular models and the simulation methods used. Then, we report and discuss the simulations of 1, 3, and 5% solutions of 1-hexanol in *n*-hexane at a temperature of 298.15 K and a pressure of 101.3 kPa. Thereafter, we discuss the results obtained from simulations of a 3% solution at temperatures ranging from 298.15 to 328.15 K. A preliminary account of simulations for the 3% solution at  $T = 298.15$  K using the optimized potentials for liquid simulations (OPLS) force field<sup>13,14</sup> has been published previously.<sup>15</sup>

## 2. Molecular Model and Simulation Methods

The simulations were carried out using the TraPPE united-atom force field,<sup>11,12</sup> which treats methyl or methylene groups as single interaction sites. The nonbonded interactions between sites on the same molecule that are separated by at least four bonds and between sites on different molecules are modeled using pairwise-additive Lennard-Jones (LJ) and Coulomb potentials. The bonded interactions include rigid bond lengths, harmonic bond-bending potentials,<sup>16,17</sup> and a truncated Fourier series for the torsional potential.<sup>13,14</sup> The potential for a site  $i$  is given by

$$U_i = \sum_{j \neq i}^{\text{sites}} \left\{ 4\epsilon_{ij} \left[ \left( \frac{\sigma_{ij}}{r_{ij}} \right)^{12} - \left( \frac{\sigma_{ij}}{r_{ij}} \right)^6 \right] + \frac{q_i q_j}{4\pi\epsilon_0 r_{ij}} \right\} + \sum_j^{\text{bonds}} \frac{k_j}{2} (\theta_j - \theta_{\text{eq},j})^2 + \sum_j^{\text{dihedrals}} \{ c_{0,j} + c_{1,j}[1 + \cos(\phi_j)] + c_{2,j}[1 - \cos(2\phi_j)] + c_{3,j}[1 + \cos(3\phi_j)] \} \quad (1)$$

where  $\epsilon_{ij}$ ,  $\sigma_{ij}$ ,  $r_{ij}$ ,  $q_i$ , and  $q_j$  are the Lennard-Jones well depth and diameter, the separation between sites, and the partial charges for sites  $i$  and  $j$ , respectively, and  $\epsilon_0$  is the vacuum permittivity.  $\theta_j$ ,  $\theta_{\text{eq},j}$ , and  $k_j$  denote the  $j$ th bond-bending angle connected to  $i$ , its equilibrium value, its and harmonic bond-bending constant, respectively.  $\phi_j$  is the  $j$ th torsional angle with  $i$  at one end, and  $c_{0,j}$ ,  $c_{1,j}$ ,  $c_{2,j}$ , and  $c_{3,j}$  are the coefficients for the corresponding truncated Fourier series used for the dihedral potential. The values of all force-field parameters are listed in Table 1.

The LJ parameters for the interactions of unlike pseudo-atoms are calculated using the standard Lorentz–Berthelot combining rules<sup>3</sup>

$$\sigma_{ij} = \frac{1}{2}(\sigma_{ii} + \sigma_{jj}) \quad \epsilon_{ij} = \sqrt{\epsilon_{ii}\epsilon_{jj}} \quad (2)$$

A spherical potential truncation for pairs of pseudo-atoms separated by more than 14 Å was enforced, and analytic tail corrections (for energies and pressures) were employed.<sup>18,19</sup> The

**TABLE 1: Bonded and Nonbonded Parameters for the TraPPE–UA Force Field**

stretch	$r_0$ (Å)			
CH <sub>x</sub> –CH <sub>y</sub>	1.54			
CH <sub>x</sub> –OH	1.43			
O–H	0.945			
bend	$\theta_0$ (°)		$k_\theta/k_B$ (K)	
CH <sub>x</sub> –(CH <sub>2</sub> )–CH <sub>y</sub>	114		62 500	
CH <sub>x</sub> –(CH <sub>2</sub> )–O	109.47		50 400	
CH <sub>x</sub> –(O)–H	108.5		55 400	
torsion	$c_0/k_B$ (K)	$c_1/k_B$ (K)	$c_2/k_B$ (K)	$c_3/k_B$ (K)
CH <sub>x</sub> –(CH <sub>2</sub> )–(CH <sub>2</sub> )–CH <sub>y</sub>	0	355.03	–68.19	791.32
CH <sub>x</sub> –(CH <sub>2</sub> )–(CH <sub>2</sub> )–OH	0	176.62	–53.34	769.93
CH <sub>x</sub> –(CH <sub>2</sub> )–(O)–H	0	209.82	–29.17	187.93
nonbonded	$\epsilon/k_B$ (K)	$\sigma$ (Å)	$q$	
CH <sub>x</sub> –(O)–H	93	3.02	–0.700	
O–(H)	–	–	+0.435	
(CH <sub>3</sub> )–CH <sub>x</sub>	98	3.75	–	
CH <sub>x</sub> –(CH <sub>2</sub> )–OH	46	3.95	+0.265	
CH <sub>x</sub> –(CH <sub>2</sub> )–CH <sub>y</sub>	46	3.95	–	

Ewald summation technique<sup>19</sup> is used to calculate the long-range Coulombic interactions, with the Ewald parameters set to  $\kappa \times L = 5$  and  $K_{\text{max}} = 5$ .

The simulated systems consisted of a total of 1000 molecules in a periodically replicated cubic box. Monte Carlo simulations were carried out in the isobaric–isothermal ensemble<sup>20</sup> using five different types of Monte Carlo moves to sample phase space efficiently. In addition to the conventional volume, translational, and rotational displacements,<sup>19</sup> the coupled–decoupled configurational-bias Monte Carlo technique<sup>21–23</sup> was used for conformational changes and for a special identity-switch move.<sup>24</sup> The latter move is necessary to sample the spatial distribution of alcohol molecules and involves the exchange of a methyl group (one interaction site) from a randomly selected alkane molecule with a (CH<sub>2</sub>)–O–H unit (three interaction sites) from a randomly selected alcohol molecule. The effectiveness of this move is demonstrated in Figure 1, which shows the trajectories of an individual alcohol molecule without and with the identity-switch move. In the former case, an alcohol molecule can become trapped in a stable aggregate so that it explores only a very local region of phase space. Using the identity-switch move, the alcohol molecule is observed to explore different parts of the simulation cell rapidly, thereby visiting free monomeric states and different aggregates. The efficient sampling of the addition and removal of alcohol molecules via the identity-switch move allows one to follow the spontaneous formation/growth and destruction/shrinkage of alcohol aggregates of varying sizes and the distribution of alcohols between different aggregates. The type of Monte Carlo move was selected at random, and a typical simulation employed 5% identity-switch moves, 0.1% volume moves, and the remainder equally divided among translational, rotational, and conformational moves.

Simulations were carried out for solutions of 1, 3, or 5 mol % 1-hexanol in *n*-hexane at  $p = 101.3$  kPa and  $T = 298.15$  K, and additional temperatures of 308.15, 318.15, and 328.15 K were investigated for the 3% solution. Each simulation was equilibrated for  $6 \times 10^4$  Monte Carlo cycles (one Monte Carlo cycle consists of  $N = 1000$  moves), and between  $5 \times 10^4$  ( $T = 328.15$  K) and  $1.3 \times 10^5$  ( $T = 298.15$  K) cycles were used for the production periods. Four independent simulations were carried out for each different system, and their results were used to calculate statistical errors.

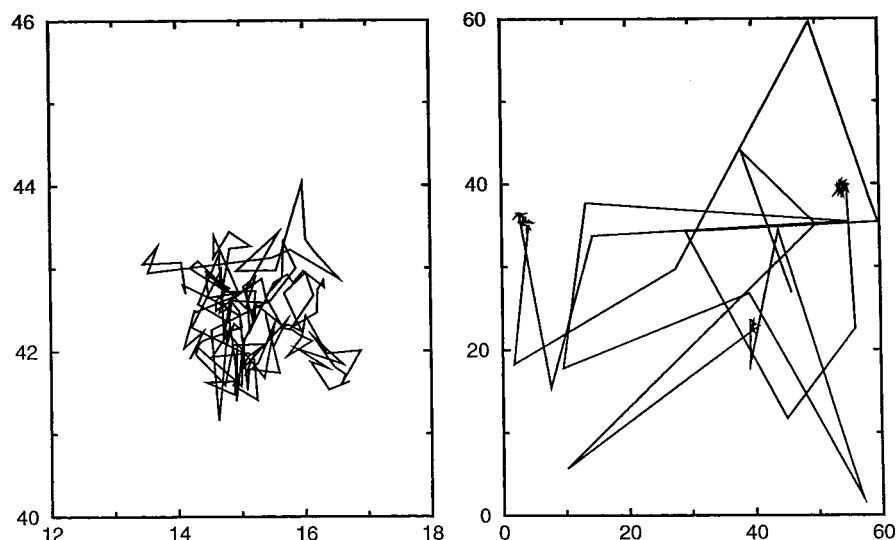


**Figure 1.** Trace of the center-of-mass motion of a single 1-hexanol molecule ( $x_{\text{OH}} = 0.03$ ,  $T = 298.15$  K) shown at intervals of 10 Monte Carlo cycles for a simulation length of 1500 Monte Carlo cycles: (left) using only regular translational, rotational, conformational, and volume moves; (right) using 5% identity-switch moves in addition to the regular moves.

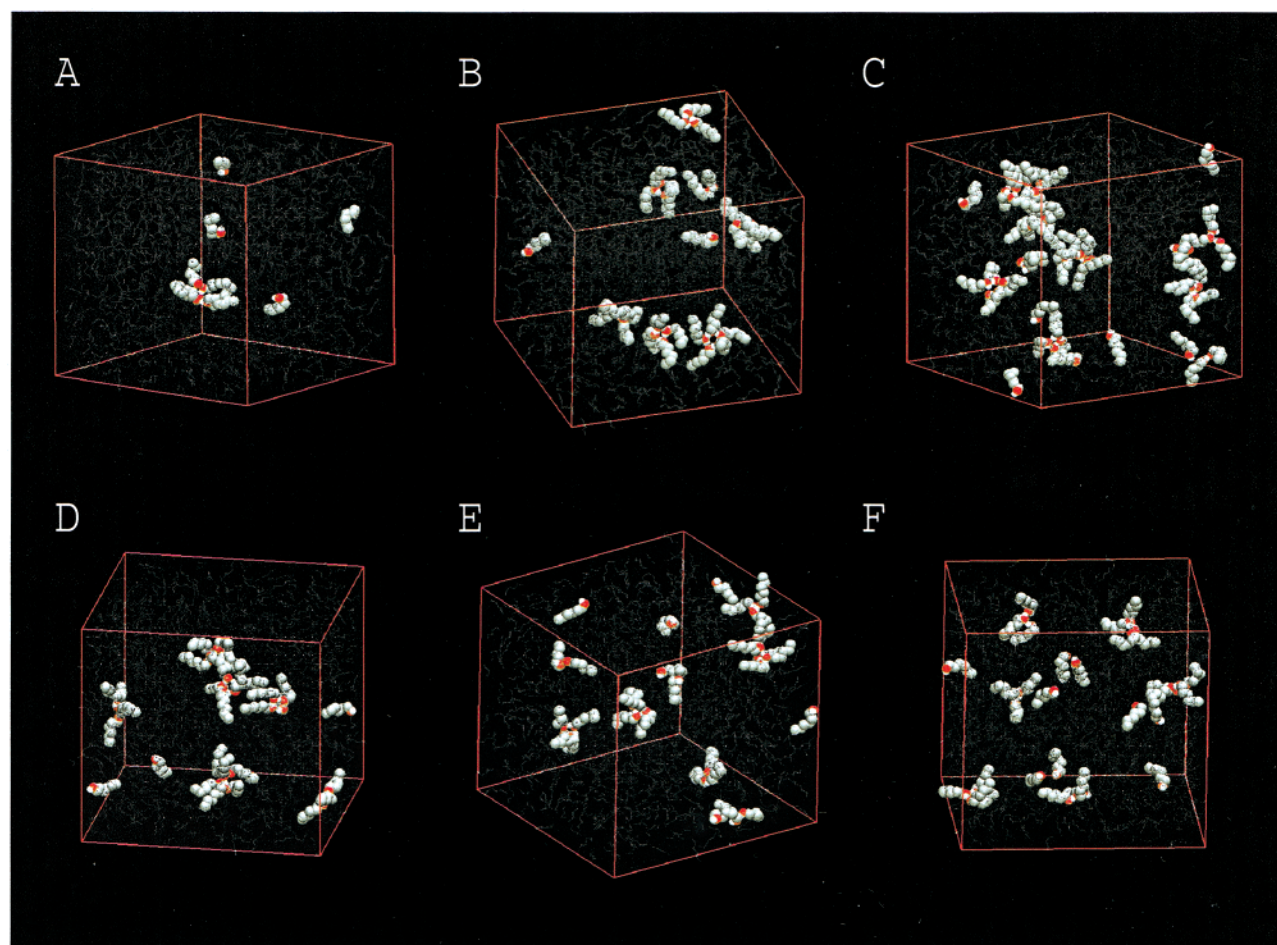


**Figure 2.** Snapshots of 1-hexanol aggregation in *n*-hexane at  $p = 101.3$  kPa and (A)  $x_{\text{OH}} = 0.01$ ,  $T = 298.15$  K; (B)  $x_{\text{OH}} = 0.03$ ,  $T = 298.15$  K; (C)  $x_{\text{OH}} = 0.05$ ,  $T = 298.15$  K; (D)  $x_{\text{OH}} = 0.03$ ,  $T = 308.15$  K; (E)  $x_{\text{OH}} = 0.03$ ,  $T = 318.15$  K; (F)  $x_{\text{OH}} = 0.03$ ,  $T = 328.15$  K. 1-Hexanol molecules are depicted by gray, red, and white spheres for methyl/methylene groups, oxygen, and hydrogen atoms, respectively, whereas a stick representation is used for the *n*-hexane solvent molecules.

### 3. Results and Discussion

**3.A. Concentration Effects.** Snapshots of the 1, 3, and 5% solutions at standard conditions ( $T = 298.15$  K and  $p = 101.3$  kPa) are shown in Figure 2 (top row). These snapshots provide a clear visual indication that the distribution of 1-hexanol

molecules is *not random* and that many of the 1-hexanol molecules form hydrogen-bonded aggregates.

Radial distribution functions (RDFs) can be used to quantify the extent of nonrandom mixing in the 1-hexanol/*n*-hexane solutions. The influence of concentration on 1-hexanol aggrega-



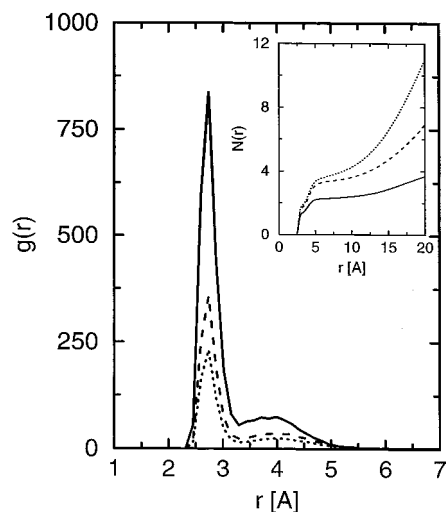


**Figure 3.** Oxygen–oxygen radial distribution functions and their corresponding number integrals (inset) at  $T = 298.15$  K and  $p = 101.3$  kPa. Solid, dashed, and dotted lines are used for 1, 3, and 5% solutions, respectively.

tion is evident from a comparison of the oxygen–oxygen RDFs and the corresponding number integrals (NIs) (see Figure 3). The height of the hydrogen-bonded peak at about  $2.8$  Å decreases substantially with increasing concentration (from about 850 for the 1% solution to about 250 for the 5% solution), i.e., the extent of nonrandom mixing decreases with increasing concentration. The heights of the second peaks at about  $4$  Å, which arise from second-nearest-neighbor molecules and are indicative of the formation of larger 1-hexanol aggregates, are much lower than the heights of the first peaks (e.g., about 100 for the 1% solution), but they are still substantially enhanced over a uniform distribution. Although the heights of the first and second peaks in the RDFs decrease with increasing concentration, the corresponding number integrals show the reverse trend. The coordination numbers for the first solvation shell ( $r_{OO} < 3.3$  Å) are 1.41, 1.78, and 1.90 for the 1, 3, and 5% solutions, respectively, i.e., even for the 1% solution, most of the 1-hexanol molecules are hydrogen-bonded to at least one other 1-hexanol molecule, and the coordination number for the 1-hexanol molecules in the 5% solution approaches the value of about 2 observed for neat liquid alcohols.<sup>12,25,26</sup>

The intermolecular hydroxyl hydrogen–oxygen RDFs for the 1, 3, and 5% solutions are shown in Figure 4. Again, the first peaks (located at about  $1.8$  Å) are indicative of strong aggregation for all concentrations, with the peak heights very close to those for the corresponding first peaks in the oxygen–oxygen RDFs. However, the second peaks in the hydrogen–oxygen RDFs (located at about  $3.2$  Å) are substantially more pronounced than those for the oxygen–oxygen RDFs because, for the hydrogen–oxygen RDFs, the first and second peaks originate from the same pair of molecules (and not from a second-nearest neighbor as for the oxygen–oxygen RDF), i.e., the second peak indicates the distance from the hydroxyl hydrogen on the acceptor molecule to the oxygen atom of the donor molecule of a hydrogen-bonded pair. The heights of the first step ( $r_{OH} < 2.5$  Å) in the corresponding NIs of 0.69, 0.87, and 0.93 for the 1, 3, and 5% solutions, respectively (see Figure 4), provide a first indication of the fraction of hydroxyl hydrogens involved in the formation of a hydrogen bond. Furthermore, the heights of the second step (which are very similar to the corresponding step heights for the oxygen–oxygen NIs) provide an estimate of the average aggregate sizes.

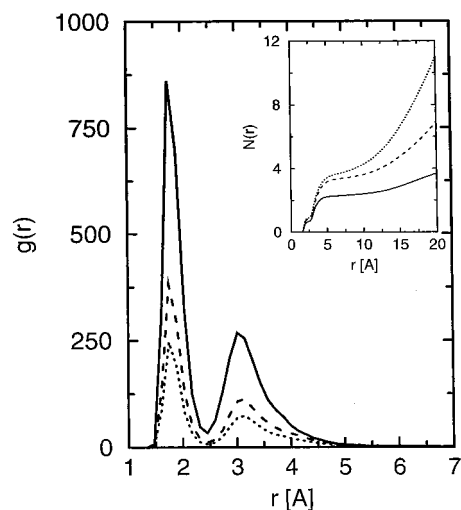


**Figure 4.** Hydroxyl hydrogen–oxygen radial distribution functions and their corresponding number integrals (oxygen atoms surrounding a given hydrogen atom, inset) at  $T = 298.15$  K and  $p = 101.3$  kPa. Line styles as in Figure 3.

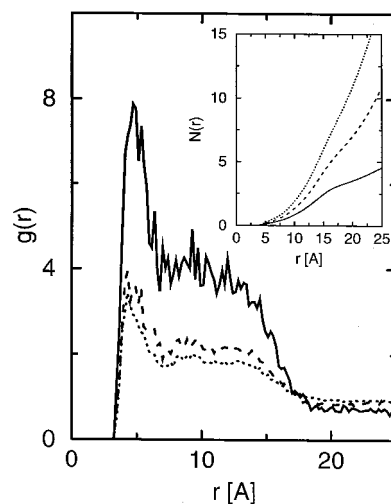


**Figure 5.**  $\omega$ -Methyl– $\omega$ -methyl radial distribution functions and their corresponding number integrals (inset) at  $T = 298.15$  K and  $p = 101.3$  kPa. Line styles as in Figure 3.

The intermolecular  $\omega$ -methyl– $\omega$ -methyl RDFs of the 1-hexanol molecules in the 1, 3, and 5% solutions are shown in Figure 5. Although the first peaks in these RDFs are about 2 orders of magnitude lower than the first peaks in the corresponding oxygen–oxygen and hydroxyl hydrogen–oxygen RDFs, there is still substantial enhancement in peak height compared to alkane liquids (see also Figure 6). The most remarkable feature of the  $\omega$ -methyl– $\omega$ -methyl RDFs is the broad shoulder that extends from about  $5$  to  $15$  Å. This shoulder is indicative of the size of the 1-hexanol aggregates found in these solutions. As the length of a 1-hexanol molecule is about  $8$  Å, a picture emerges in which the aggregates consists of an inner hub of hydroxyl groups with spokes of alkyl tails that extend outward. These hub-and-spoke structures are also clearly visible in the snapshots shown in Figure 2. The low values of the NIs for separations smaller than  $6$  Å show that very few of the alkyl tails of a given aggregate assume a parallel orientation. Furthermore, the values of the NIs for the  $\omega$ -methyl– $\omega$ -methyl RDFs at  $15$  Å are very similar to those of the oxygen–oxygen RDFs, which signals that, for the three concentrations studied here, most of the aggregates are isolated, with very little interdigitation between aggregates.

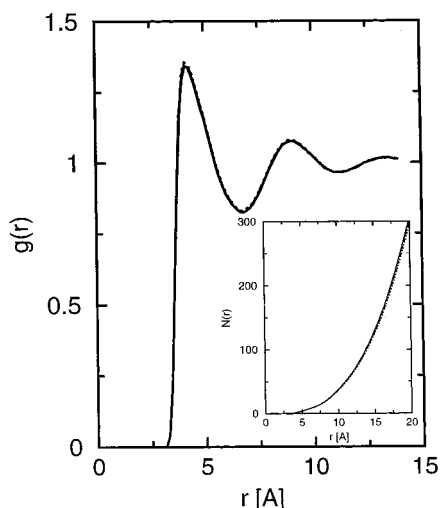


**Figure 6.** Intermolecular hexane methyl-hexane methyl radial distribution functions and their corresponding number integrals (inset) at  $T = 298.15$  K and  $p = 101.3$  kPa. Line styles as in Figure 3.

The intermolecular methyl-methyl RDFs of the *n*-hexane molecules in the 1, 3, and 5% solutions are shown in Figure 6. These RDFs show the typical signatures of a relatively disordered alkane liquid. Most important is that the RDFs for the three concentrations are nearly indistinguishable, i.e., the structures of the *n*-hexane solvent molecules are not disturbed by the formation of the 1-hexanol aggregates.

Although the RDFs discussed above provide a semiquantitative description of the aggregation behavior in the 1-hexanol solutions, a more precise definition of hydrogen bonding is required before the aggregates can be further investigated. In particular, in simulation studies using empirical force fields that employ a combination of Coulombic interactions and the repulsive part of the Lennard-Jones potential to mimic hydrogen bonding, there is a certain ambiguity in deciding whether a donor hydrogen and an acceptor oxygen in close proximity are sufficient to constitute a hydrogen bond. Even in experimental studies or ab initio calculations, a clear-cut distinction of hydrogen bonding does not exist. For example, in FTIR studies on 1-hexanol/*n*-hexane solutions, it was observed that there is some overlap between the peak associated with a free O-H stretch and the bound O-H stretch, and a peak-deconvolution algorithm had to be used to quantify the extent of free O-H stretches.<sup>9</sup>

To determine the best hydrogen-bonding criteria for the simulations described here, the structure of 1-hexanol molecules in the 3% solution at  $T = 298.15$  K was further analyzed. Figure 7 shows two-dimensional histograms of the number of 1-hexanol pairs as a function of the hydroxyl hydrogen-oxygen distance and of the cosine of the angle formed by the bond vector from the hydroxyl hydrogen to the oxygen atom on the first molecule and by the bond vector from the (fictitious) lone-pair site to the oxygen atom of the second molecule in the pair. The positions of the two lone pairs were determined using a "bond length" of  $0.5$  Å and a tetrahedral arrangement with respect to the carbon and hydrogen bonded to the oxygen, and the lone pair that is closer to the hydroxyl hydrogen of the first molecule was taken for the calculation of the hydrogen-bond angle. It should be noted that the lone pairs are used exclusively for the purpose of this analysis and are not part of the force field used during the simulations. Figure 7 can be interpreted to give structural information regarding the hydrogen-bonded aggregates. Three distinct peaks are present, the first at  $1.5$  Å  $< r_{OH} < 2.5$  Å and  $-1 < \cos \theta_{OH \cdots OL} < -0.4$ , the second at  $2.5$

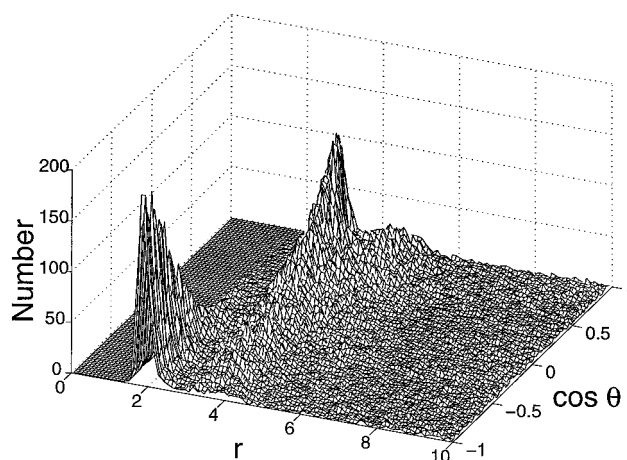


**Figure 7.** Distribution of oxygen-hydrogen pairs ( $x_{OH} = 0.03$ ,  $T = 298.15$  K) as a function of their separation (in Å) and of the cosine of the angle between the oxygen-hydrogen bond of the donor molecule and the oxygen-lone pair "bond" of the acceptor molecule.

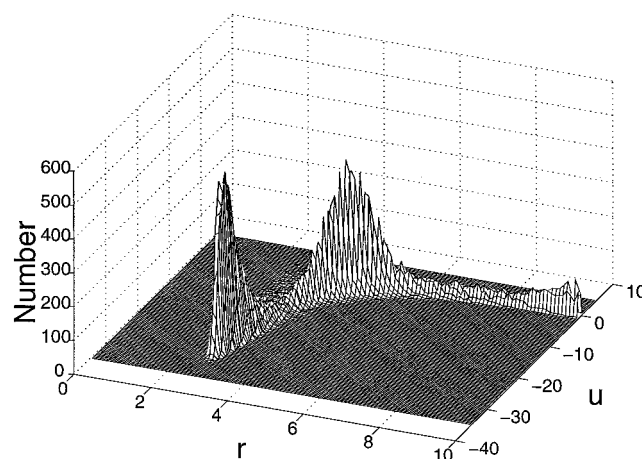


**Figure 8.** Distribution of oxygen-oxygen pairs ( $x_{OH} = 0.03$ ,  $T = 298.15$  K) as a function of their separation (in Å) and of the interaction energy (in kJ/mol) between the ( $CH_2$ -O-H) groups.

Å  $< r_{OH} < 3.5$  Å and  $0 < \cos \theta_{OH \cdots OL} < 1$ , and the third at  $3.5$  Å  $< r_{OH} < 5.5$  Å and  $0 < \cos \theta_{OH \cdots OL} < 1$ . The first peak arises from a geometry in which the hydrogen is not only close to the neighboring oxygen but the hydrogen bond is nearly linear with respect to one of that oxygen's lone pairs. The second peak, nearly as high as the first, is a consequence of the fact that, for each 1-hexanol pair that has one hydrogen and oxygen contributing to the first peak, the remaining hydrogen and oxygen will be slightly further apart and, because of the approximately tetrahedral geometry of the oxygen center, will have a hydrogen-lone pair angle that is close to zero. The third peak, broad in comparison to the first two, indicates a more nonspecific interaction that is expected from second-nearest-neighbor alcohols in an aggregate formed by at least three 1-hexanol molecules.

In Figure 8, the 1-hexanol pairs are sorted according to the oxygen-oxygen distance and the intermolecular interaction,  $u_{head}$ , of the two headgroups. This energy was determined from the Lennard-Jones interactions between intermolecular oxygen and  $\alpha$ -carbon sites and Coulombic interactions between intermolecular hydrogen, oxygen, and  $\alpha$ -carbon sites. The main features of this histogram are two large peaks, the first located at  $2.5$  Å  $< r_{OO} < 3.3$  Å and  $-30$  kJ/mol  $< u_{head} < -13$  kJ/mol and the second located at  $3.3$  Å  $< r_{OO} < 5.5$  Å and  $-13$  kJ/mol  $< u_{head} < 0$  kJ/mol. The first peak, arising from the nearest-

**TABLE 2: Percentages of Free O–H Bonds and Fractions of Monomeric 1-Hexanol Molecules**

$x_{\text{OH}}$ (%)	$T$ (K)	$f_{\text{freeO-H}}^{\text{FTIR}}$ (%)	$f_{\text{freeO-H}}^{\text{LFHB}}$ (%)	$f_{\text{freeO-H}}^{\text{SIM}}$ (%)	$f_{\text{monomer}}^{\text{SIM}}$ (%)
1.00	298.15	—	65.0	$44.5 \pm 1.6$	$32.6 \pm 1.8$
1.31	298.15	57.0	56.1	—	—
3.00	298.15	32.7	33.2	$27.3 \pm 0.8$	$14.9 \pm 0.8$
5.00	298.15	—	23.5	$22.3 \pm 1.0$	$9.9 \pm 0.7$
3.00	308.15	—	40.8	$32.1 \pm 1.0$	$18.8 \pm 1.2$
3.07	308.15	41.7	40.2	—	—
3.00	318.15	—	—	$38.2 \pm 1.3$	$25.4 \pm 1.0$
3.00	328.15	—	—	$44.2 \pm 0.8$	$31.9 \pm 0.9$

neighbor interactions of hydrogen-bonded pairs, is well separated from the second peak, which has a comparatively low interaction energy and is due to second-nearest neighbors in larger aggregates. Because of the distributions shown in Figures 7 and 8, a hydrogen bond was determined to exist between two alcohol molecules if it satisfied *all* of the following criteria:  $r_{\text{OO}} \leq 3.3$  Å,  $r_{\text{OH}} \leq 2.5$  Å,  $\cos \theta_{\text{OH} \cdots \text{OL}} \leq -0.4$ , and  $u_{\text{head}} \leq -13$  kJ/mol.

Using the definition for hydrogen bonding given above, the aggregation behavior in the 1-hexanol/*n*-hexane solutions was first analyzed with respect to the fractions of free hydroxyl hydrogens (that are not involved as donors in a hydrogen bond) and monomeric 1-hexanol molecules (that do not participate in any hydrogen bond). It is well documented that an alcohol molecule that acts as a hydrogen-bond acceptor but not also as a donor, i.e., whose own hydrogen is not participating in a hydrogen bond, will be indistinguishable from a true monomeric alcohol by both FTIR and NMR spectroscopy.<sup>27,28</sup> Therefore, comparisons to experimental measurements of hydrogen bonding<sup>9</sup> are made best using the fraction of free hydroxyl hydrogens and not the fraction of monomers. The simulation results for these two quantities and the experimental FTIR data are summarized in Table 2, along with the predictions of the extended lattice-fluid hydrogen-bonding (LFHB) theory that includes hydrogen-bond cooperativity by using separate equilibrium constants for dimer-like and polymer-like hydrogen bonds.<sup>9</sup> As was demonstrated by Gupta and Brinkley,<sup>9</sup> a value of 10 for the ratio between the polymer-like and dimer-like equilibrium constants allows for an excellent fit to the experimental data. In contrast, there are substantial deviations between the experimental and simulation data. In particular, for the 1% solution, the simulations predict that less than half of the hydroxyl hydrogens are not involved in the formation of a hydrogen bond, whereas the experimental data and LFHB theory put this number at about two-thirds. However, the deviations between experiment/LFHB theory and simulation appear to become smaller as the alcohol concentration increases. Here, we can only speculate on the causes of the deviation between experiment and simulation. Clearly, the use of an even stricter hydrogen-bond criterion for the analysis of the simulation data could help. However, the fact that the deviation diminishes with increasing alcohol concentration makes the use a nonpolarizable force field the most likely culprit. The TraPPE–UA force field for the alcohols uses partial charges that reproduce the properties of bulk alcohols,<sup>12,14</sup> i.e., to account for induced polarization effects, the dipole moment of the model is significantly enhanced over that measured for isolated alcohols in the gas phase. Thus, the TraPPE–UA model is expected to work best for cases where the majority of alcohols are involved in aggregation (e.g., the fraction of free hydroxyl hydrogens in the 5% solution is only about 20%) because the extent of induced polarization in these aggregates would be similar to that observed for bulk liquid alcohols.<sup>6–8</sup> In contrast, the extent of hydrogen bonding predicted by the TraPPE–UA force field should be too large at low alcohol concentrations because the enhanced partial

charges favor aggregation. Although only a simulation study using polarizable alcohol and alkane models (which is beyond our current computational facilities) will be able to address these issues satisfactorily, the importance of the specific values of the partial charges can be demonstrated by using a nonpolarizable alcohol model with reduced partial charges. Thus, another simulation of the 3% solution was carried out using the Lennard-Jones parameters of the TraPPE–UA force field with the CM2 charges determined from the SM5.4 solvation model<sup>29,30</sup> for an isolated 1-hexanol molecule solvated in *n*-hexane ( $q_{\text{H}} = +0.336e$ ,  $q_{\text{O}} = -0.514e$ , and  $q_{\alpha\text{-CH}_2} = +0.178e$ ). This reduced-charge model resulted in a dramatic reduction of the fraction of 1-hexanol aggregates, and the fraction of free hydroxyl hydrogens jumped to more than 90%, i.e., it deviated from the experimental measurements in the opposite direction than the TraPPE–UA model.

The simulations also reveal that the fraction of free 1-hexanol molecules is significantly smaller than the fraction of free hydroxyl hydrogens (see Table 2). As is well-known from studies of neat liquid alcohols,<sup>12,25,26</sup> steric hindrance effectively limits the accessibility of the lone-pair sites on an alcohol, and usually only one of these acceptor sites is involved in the formation of a hydrogen bond at any given time. In a similar manner, linear and cyclic aggregates dominate for the aggregates found in the 1-hexanol/*n*-hexane solutions (see Table 3). Because all linear aggregates contain one hydrogen bond less than their aggregate size, the fraction of free hydroxyl hydrogens exceeds the fraction of free 1-hexanol molecules.

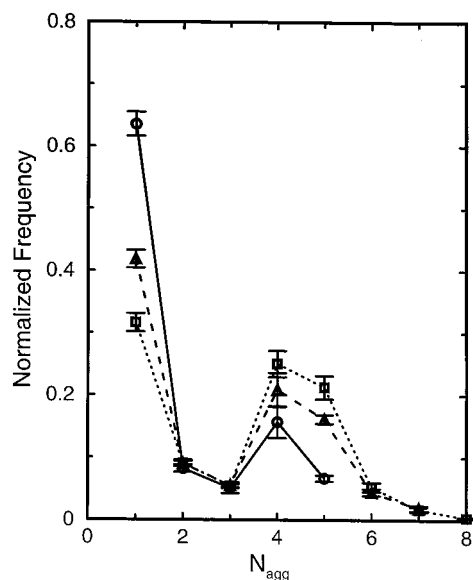
The distribution of cluster sizes (aggregation numbers) and types (linear, cyclic, or branched) is one of the most important properties in the description of associating fluids. Whereas the experimental determination of these microscopic properties is rather difficult, they can be simply calculated from configuration files generated throughout a simulation. The effect of concentration on the aggregation behavior is shown in Figure 9, which displays the fraction of aggregates as a function of aggregation size. The distribution over aggregation sizes can be normalized in two principle ways: either using the total number of aggregates in a given configuration or using the total number of molecules. The former is used here because it allows for the direct calculation of equilibrium constants between aggregates. However, it should be noted that, although the fraction of all clusters of size 1 is about 0.42 for the 3% solution, the fraction of molecules that are monomers is only about 0.15 (see Table 2). Similarly, the fraction of molecules that participates in tetramers and pentamers is larger than the fraction that consists of monomers. A bimodal distribution is observed in Figure 9 for all three concentrations, with a large number of monomeric species, fewer dimers and trimers, and a large number of tetramers and pentamers, beyond which the distribution tails off. The pronounced dips for dimers and trimers are evidence for the importance of cooperativity in hydrogen bonding.<sup>31</sup> The predominant aggregation sizes are 4 and 5, in agreement with previous NMR studies by Karachewski et al.<sup>27</sup> for mixtures of 2-propanol in *n*-heptane and 1-butanol in cyclohexane. Only very few aggregates consisting of more than five alcohols were found for the 1% solution, which might be caused by a system size effect as the 1% solution contained only a total of 10 1-hexanol molecules. Overall, the effect of an increasing 1-hexanol concentration is a decrease of the fraction of monomeric species but an increase of the fraction of larger aggregates (consisting of four or more alcohol molecules).

The average numbers of hydrogen bonds and fractions of different aggregate architectures are reported in Table 3. Every



**TABLE 3: Average Numbers of Hydrogen Bonds and Fractions of Cyclic, Linear, and Branched Aggregates at  $T = 298$  K**

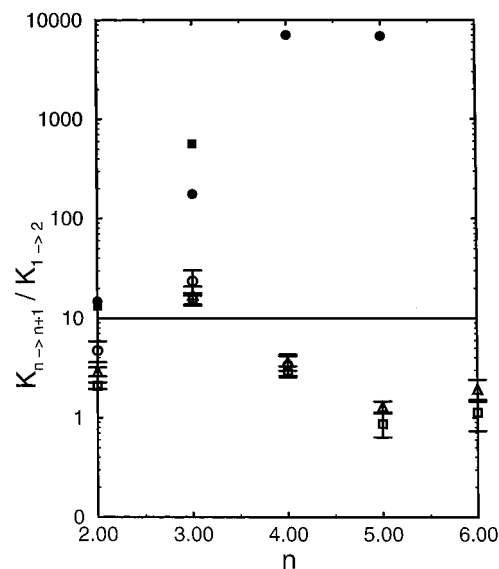
$N_{\text{agg}}$	$n_{\text{HB}}^{1\%}$	$f_{\text{cyc}}^{1\%}(\%)$	$f_{\text{lin}}^{1\%}(\%)$	$f_{\text{bra}}^{1\%}(\%)$	$n_{\text{HB}}^{3\%}$	$f_{\text{cyc}}^{3\%}(\%)$	$f_{\text{lin}}^{3\%}(\%)$	$f_{\text{bra}}^{3\%}(\%)$	$n_{\text{HB}}^{5\%}$	$f_{\text{cyc}}^{5\%}(\%)$	$f_{\text{lin}}^{5\%}(\%)$	$f_{\text{bra}}^{5\%}(\%)$
3	2.04	4	96	0	2.02	2	98	0	2.01	1	99	0
4	3.54	53	47	0	3.50	50	50	0	3.51	51	49	0
5	4.62	59	37	4	4.55	54	43	3	4.58	54	41	5
6					5.56	46	41	13	5.50	40	44	16

**Figure 9.** Distribution of hydrogen-bonded clusters over aggregation sizes. Circles, triangles, and squares depict the simulation results for 1, 3, and 5% solutions, respectively.

dimer found contained only a single hydrogen bond, and the overwhelming majority of trimers contained only two hydrogen bonds (remember that the definition of a hydrogen bond includes an angular cutoff for the hydrogen-bond angle). In contrast, the average numbers of hydrogen bonds for all larger aggregates is about  $n - 0.5$ , i.e., approximately half of these aggregates contain one hydrogen bond per molecule, allowing for closed cyclic structures. The presence of these cyclic structures for alcohol aggregates in alkane solvents was already inferred in a previous experimental study,<sup>27</sup> and the ab initio calculations of Sum and Sandler<sup>10</sup> clearly point to more favorable binding energies for cyclic alcohol clusters. The formation of cyclic clusters with aggregation sizes of 4 or greater requires relatively little strain of the hydrogen-bonded network. Thus, we also analyzed the fraction of molecules with respect to cluster architecture. Three types were considered: cyclic, linear, and branched (see Table 3). The cluster architecture was assigned by the following rules: (i) if a cluster contains a molecule that is bonded to more than two neighbors, it is branched; (ii) if a cluster contains only molecules with exactly two neighbors, it is a (monocyclic) ring; and (iii) otherwise, it is a linear cluster. In agreement with the hydrogen-bonding cooperativity argument, it was observed that cyclic architectures are important and make up about half of the clusters containing between four and six molecules. However, linear architectures seem to be of similar importance. Branched architectures start to emerge for hexamers and larger clusters. The effect of changing composition (from 1 to 5%) on the cluster architectures appears to be insignificant.

The equilibrium constant for the formation of an  $n$ -mer from monomers is given by

$$K_n = \frac{x_n}{(x_1)^n} \quad (3)$$

**Figure 10.** Equilibrium constant ratios for alcohol aggregates. The solid line is the ratio determined from a fit of the LFHB theory to the experimental data by Gupta and Brinkley.<sup>9</sup> Filled circles and squares represent the results of the Hartree–Fock calculations for cyclic clusters by Sum and Sandler<sup>10</sup> for methanol and 1-propanol, respectively. Open circles, triangles, and squares depict the simulation results for the 1, 3, and 5% solutions, respectively.

where  $x$  is the fraction of clusters of a given size. In addition, a useful measure of hydrogen-bond cooperativity is the ratio of the equilibrium constant of forming a multimer hydrogen bond to that of forming a dimer hydrogen bond

$$\frac{K_{n \rightarrow n+1}}{K_{1 \rightarrow 2}} = \left( \frac{x_{n+1}}{x_1 x_n} \right) \left( \frac{(x_1)^2}{x_2} \right) = \frac{x_{n+1} x_1}{x_n x_2} \quad (4)$$

Figure 10 shows a comparison of the equilibrium constant ratios determined from the simulations for the 1, 3, and 5% solutions to both the fitted parameter from the LFHB theory<sup>9</sup> and the values estimated from the ab initio calculations for methanol and 1-propanol clusters.<sup>10</sup> First, both the simulations and the ab initio calculations clearly demonstrate that a single equilibrium constant ratio is insufficient to describe the hydrogen-bond cooperativity in these solutions. However, the ab initio calculations yield equilibrium constant ratios that increase monotonically with aggregate size, whereas the simulation data indicate a maximum for the formation of the tetramer and decreasing ratios for the larger clusters. The bimodal distributions over aggregate sizes observed in the simulations (see Figure 9) are a direct consequence of the maximum in the equilibrium constant ratios. In contrast, monotonically increasing equilibrium constant ratios would lead to macroscopic phase separation, which is not observed experimentally for the 1-hexanol/ $n$ -hexane solutions studied here. As emphasized by Sum and Sandler,<sup>10</sup> their calculations of equilibrium constant ratios from ab initio energies involve the assumption that the change in entropy due to the addition of one molecule to a hydrogen-bonded aggregate is independent of the aggregate size. Whereas this assumption

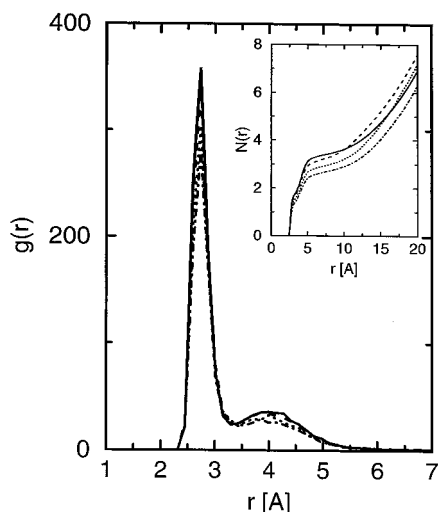


**Figure 11.** Oxygen–oxygen radial distribution functions and their corresponding number integrals (inset) for a 3% solution at  $p = 101.3$  kPa. Solid, dashed, dotted, and dashed–dotted lines are used for  $T = 298.15, 308.15, 318.15,$  and  $328.15$  K, respectively.

might work for linear aggregates, the change of entropy on forming small cyclic structures should be different because these small cyclic structures are constrained and exhibit significantly less conformational entropy.

In addition, as should be expected from the effects of concentration on the distribution over aggregation sizes (i.e., decreasing fraction of larger aggregates with decreasing concentration, see Figure 9), the equilibrium constant ratios show some concentration dependence. The equilibrium constant ratios for trimer and tetramer formation are slightly larger for the 1% solution because of the increase of  $x_1$  in the numerator of eq 4.

**3.B. Temperature Effects.** Temperature plays an important role in aggregation behavior because aggregate formation is usually driven by the favorable enthalpy of adding another molecule to a cluster (resulting, for example, in an increase in the number of hydrogen bonds), whereas entropic factors usually favor the dissociation of aggregates into monomers. Snapshots of the 3% solution at three additional temperatures ( $T = 308.15, 318.15,$  and  $328.15$  K) are shown in Figure 2 (bottom row). Increasing the temperature further (at  $p = 101.3$  kPa) would lead to vapor–liquid coexistence with an *n*-hexane-rich vapor phase.<sup>32,33</sup>

Figures 11 and 12 show, respectively, the oxygen–oxygen and hydroxyl hydrogen–oxygen RDFs and NIs for the 3% solution at the four temperatures studied. With increasing temperature, the heights of the first and second peaks in the RDFs decrease, as do the plateau heights in the corresponding NIs, i.e., there is less aggregate formation, and the average aggregate size decreases. However, the observed temperature response is not as dramatic as the concentration effects. Part of the reason is certainly that the temperature was only varied by 10% (from 298.15 to 328.15 K) whereas the concentrations differed by a factor of 5 (from 1 to 5%), i.e., the normalizing number densities for the RDFs are more similar for the different temperatures than for the different concentrations.

The distributions over aggregation sizes for the four temperatures are presented in Figure 13. As expected, the fraction of monomers increases, and the fraction of larger aggregates decreases with increasing temperature, although the bimodal character of the distribution remains in force over the entire temperature range. It is noteworthy that the distributions over aggregation sizes are remarkably similar for the 1% solution at

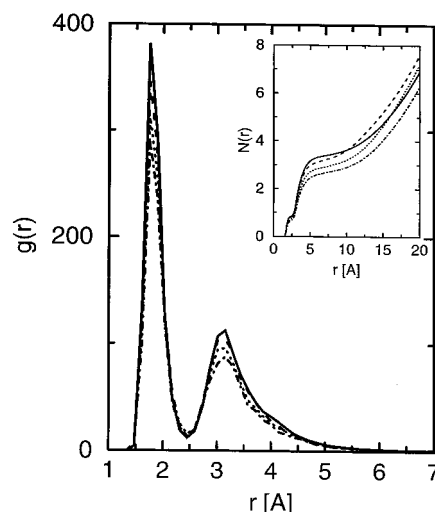


**Figure 12.** Hydroxyl hydrogen–oxygen radial distribution functions and their corresponding number integrals (oxygen atoms surrounding a given hydrogen atom, inset) for a 3% solution at  $p = 101.3$  kPa. Line styles as in Figure 10.

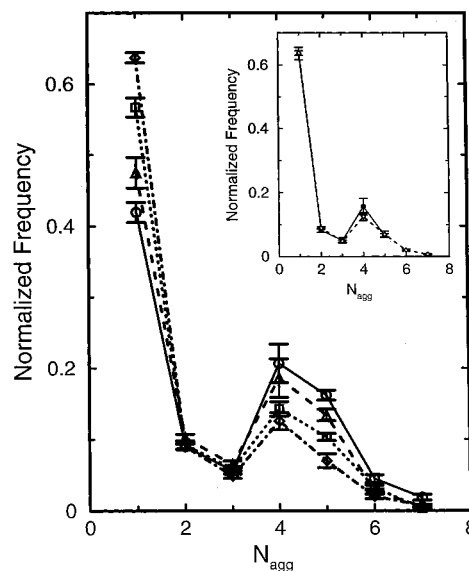


**Figure 13.** Distribution of hydrogen-bonded clusters over aggregation sizes for the 3% solution. Circles, triangles, squares, and diamonds are used for the simulation results at  $T = 298.15, 308.15, 318.15,$  and  $328.15$  K, respectively. The inset shows a comparison for the 1% solution at  $T = 298.15$  K (filled circles) and the 3% solution at  $T = 328.15$  K (diamonds).

$T = 298.15$  K and the 3% solution at  $T = 328.15$  K (see inset of Figure 13), despite the large differences in their RDFs (the heights of the first peaks in the oxygen–oxygen RDFs are about 850 and 280, respectively).

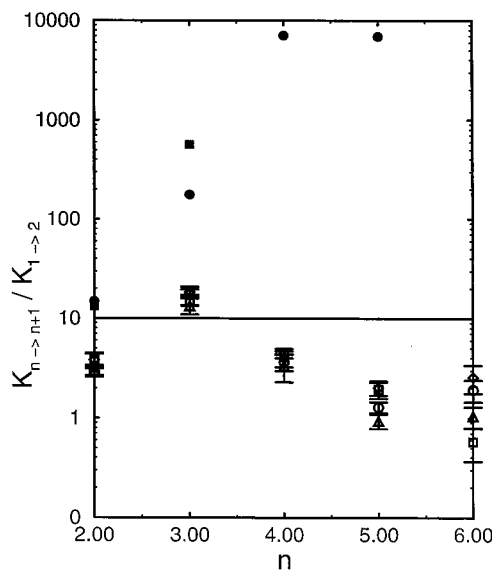
For the 3% systems at different temperatures, the average numbers of hydrogen bonds and the fractions of aggregate architectures are given in Table 4. Although one might expect that entropic arguments would favor linear and branched architectures, resulting in a reduction of the average number of hydrogen bonds for a given aggregation number, neither quantity shows a significant temperature effect, which indicates that, although the equilibrium constants shift as a function of temperature, no significant structural changes of the aggregate architectures occur.

Figure 14 shows a comparison of the equilibrium constant ratios determined from the simulations for the 3% solutions at the four different temperatures to the fitted parameter from the



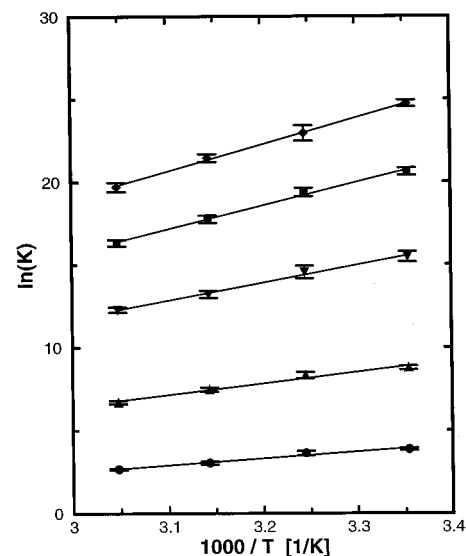
**TABLE 4: Average Numbers of Hydrogen Bonds and Fractions of Cyclic, Linear, and Branched Aggregates for 3% Solutions**

$N_{\text{agg}}$	$n_{\text{HB}}^{308}$	$f_{\text{cyc}}^{308}(\%)$	$f_{\text{lin}}^{308}(\%)$	$f_{\text{bra}}^{308}(\%)$	$n_{\text{HB}}^{318}$	$f_{\text{cyc}}^{318}(\%)$	$f_{\text{lin}}^{318}(\%)$	$f_{\text{bra}}^{318}(\%)$	$n_{\text{HB}}^{328}$	$f_{\text{cyc}}^{328}(\%)$	$f_{\text{lin}}^{328}(\%)$	$f_{\text{bra}}^{328}(\%)$
3	2.02	3	97	0	2.02	2	98	0	2.04	4	96	0
4	3.50	49	51	0	3.47	47	53	0	3.49	49	50	1
5	4.56	54	42	4	4.57	55	39	6	4.54	52	42	6
6	5.43	27	50	23	5.48	36	51	13	5.58	47	39	14

**Figure 14.** Equilibrium constant ratios for alcohol aggregates. Solid line and filled symbols as in Figure 10. Open circles, triangles, squares, and diamonds are used for the simulation results at  $T = 298.15, 308.15, 318.15,$  and  $328.15$  K, respectively.

LFHB theory<sup>9</sup> and the values estimated from the ab initio calculations for methanol and 1-propanol clusters.<sup>10</sup> As emphasized above, the simulations yield different equilibrium constant ratios as a function of aggregation number, with a maximum for the formation of the tetramer. The temperature effects are smaller than the concentration effects, but the temperature was only changed by a modest 10%. This is in agreement with the fact that the same equilibrium constant ratio between dimer-like and polymer-like hydrogen bonds could be used for the LFHB theory to fit the experimental data at  $T = 298.15$  and  $308.15$  K.<sup>9</sup>

**3.C. Thermodynamic Quantities.** In certain favorable cases, it is possible to determine the enthalpies of aggregate formation directly from configuration files produced during simulations. A good example is the aggregation of hydrogen fluoride in its superheated vapor phase,<sup>34</sup> where the internal energy change of aggregate formation is given by the intermolecular interactions of the molecules in the aggregate (assuming that clusters are independent entities) and where the volume change of aggregate formation can be approximated by the corresponding ideal-gas term. However, the situation is much more complicated for solutions of flexible molecules such as those studied here. First, the change in intermolecular interactions with the solvent environment would need to be considered too, but a clear rule as to which solvent molecules to include does not exist. (The situation would be greatly simplified if only one aggregate were present in the simulated system and all solvent molecules were considered.) Second, the average conformation of a solute molecule might depend on aggregate size, and thus, the changes in intramolecular energy would contribute to the enthalpy of cluster formation. Third, the calculation of the  $p\Delta V$  term would require knowledge of the partial molar volumes for the different aggregates, although this term should be rather small for liquid solutions at atmospheric pressure. Therefore, the conventional

**Figure 15.** van't Hoff plots used for the determination of the enthalpies of cluster formation. Circles, upward triangles, downward triangles, squares, and diamonds depict the results for clusters with aggregation numbers of 2, 3, 4, 5, and 6, respectively. Linear fits are shown as thin solid lines.

thermodynamic route was followed, i.e., simulations were carried out at different temperatures, and the van't Hoff equation was used to determine the enthalpies of aggregate formation from the temperature dependence of the equilibrium constants via

$$\left[ \frac{\partial \ln K_n}{\partial (1/T)} \right]_p = \frac{\Delta H_n}{R} \quad (5)$$

It should be noted here that the enthalpy of hydrogen-bond formation,  $\Delta H_{\text{hb}}$ , differs from the enthalpy of aggregate formation,  $\Delta H_n$ , because the average number of hydrogen bonds for a given aggregate size is always smaller than the size itself (because of the presence of linear and branched aggregates). However, because the temperature dependence of the average number of hydrogen bonds is very weak (see Table 4), the calculation of  $\Delta H_{\text{hb}}$  is straightforward once  $\Delta H_n$  is known.

Figure 15 shows the van't Hoff plots for aggregates up to hexamers. For all cases, the calculated equilibrium constants follow the van't Hoff equation to within their statistical uncertainties. As seen for the equilibrium constant ratios (see Figure 14), the enhanced stability of the tetramer manifests itself in a larger jump from the trimer to the tetramer equilibrium constants.

The values of  $\Delta H_n^*$  per molecule and of  $\Delta H_{\text{hb}}^*$  per hydrogen bond as functions of aggregation number are presented in Figure 16, along with the total binding energies for methanol clusters determined at the Hartree–Fock level (the corresponding MP2 energies are about 30% larger in magnitude).<sup>10</sup> A striking outcome of the simulations is that the magnitude of  $\Delta H_n^*$  increases with increasing aggregation size, whereas the mag-

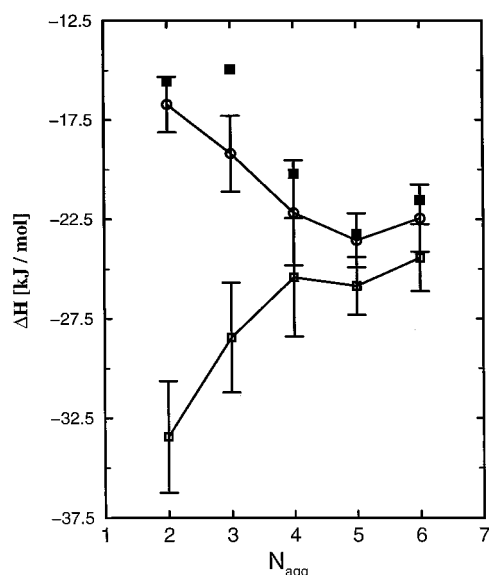


**Figure 16.** Enthalpies of aggregate formation per molecule (circles) and of hydrogen-bond formation (squares) as functions of the aggregation number. Open and filled symbols are used for the simulation results (this work) and the Hartree-Fock calculations for cyclic methanol clusters by Sum and Sandler,<sup>10</sup> respectively.

nitude of  $\Delta H_{\text{hb}}^*$  decreases. The former can be attributed to two causes: (i) the favorable dipole-dipole interactions between 1-hexanol molecules that are not directly hydrogen-bonded but belong to the same aggregate and (ii) the ability of the larger clusters to form cyclic structures, which increases the average number of hydrogen bonds per molecule (see Tables 3 and 4). Although cyclic structures possess one hydrogen bond per molecule, the hydrogen-bond angle is strained in particular for the smaller aggregates, which might explain the decrease in the magnitude of  $\Delta H_{\text{hb}}^*$ . Furthermore, the less favorable  $\Delta H_n^*$  and  $\Delta H_{\text{hb}}^*$  values for the hexamer (albeit well within the statistical noise) could be a signature of the increasing fraction of aggregates with branched architectures, where steric effects would weaken the strengths of the hydrogen bonds at the branch point. These results agree to some extent with the findings of the ab initio calculations by Sum and Sandler,<sup>10</sup> who found that the magnitudes of the binding energies per hydrogen bond for cyclic clusters decrease from dimer to trimer and then increase up to pentamers, followed by a decrease for the hexamer. The hydrogen-bond criteria used in this work are rather strict, and for example, the cyclic trimer found in the ab initio calculations does not satisfy these criteria, which makes a direct comparison of the simulation data and ab initio energies difficult. However, it should be emphasized that a polarizable force field should yield a much enhanced cooperativity effect compared to the nonpolarizable TraPPE-UA force field.<sup>8</sup>

The enthalpy of hydrogen-bond formation for a dilute solution of 1-butanol in cyclohexane was estimated by Karachewski et al.,<sup>27</sup> who measured the chemical shift of the hydroxyl proton via nuclear magnetic resonance at various concentrations and fit the results to three different association models. The values of the enthalpy of hydrogen-bond formation ranged from -28 to -38 kJ/mol for the three different models, i.e., the results were similar in magnitude to the values of  $\Delta H_{\text{hb}}^*$  found in the simulations for dimers, but larger in magnitude than the simulation results for the larger clusters, which are close to -25 kJ/mol.

The incremental Gibbs free energies and enthalpies for the addition of a monomer to a cluster of size  $n$  are summarized in

**TABLE 5: Thermodynamic Quantities for 1-Hexanol Aggregates in the 3% Solution at  $T = 298$  K and Hartree-Fock Binding Energies<sup>10</sup>**

$n$	$\Delta\Delta G_{n \rightarrow n+1}$ (kJ/mol)	$\Delta\Delta H_{n \rightarrow n+1}$ (kJ/mol)	$\Delta\Delta U_{n \rightarrow n+1}$ (kJ/mol)
2	$-12.2 \pm 0.4$	$-24 \pm 6$	-29.3
3	$-16.6 \pm 0.8$	$-31 \pm 12$	-36.1
4	$-12.8 \pm 1.0$	$-29 \pm 13$	-35.3
5	$-10.2 \pm 0.8$	$-17 \pm 12$	-13.1

Table 5. As already discussed for the equilibrium constant ratios (see Figures 10 and 14), the free energy for the formation of the tetramer is most favorable. Perhaps somewhat surprising is that the same pattern is also reflected in the enthalpy changes, i.e., the enthalpy of adding a fourth molecule to a trimer is larger in magnitude than the enthalpy for the formation of a trimer or a hexamer. The difference from trimer formation is clearly related to a reduction in the ring strain of the tetramer (more favorable hydrogen-bond angles), as was also found in the ab initio calculations of Sum and Sandler.<sup>10</sup> The origin of the smaller enthalpy gain for the formation of the hexamer is less obvious, albeit Sum and Sandler also observed a significant decrease in the incremental binding energy for the formation of the cyclic hexamer (see Table 5). As noted above, a significant fraction of the hexamers found in the simulations exhibit a branched architecture for which the hydrogen-bond strength at the branch site might be weakened.

#### 4. Conclusions

In this paper, the results of configurational-bias Monte Carlo simulations in the isobaric-isothermal ensemble for the aggregation behavior of 1-hexanol in dilute solutions in *n*-hexane are reported. The use of a special identity-switch move allowed for efficient sampling of the spatial distribution of 1-hexanol molecules and, in particular, for the addition/removal of 1-hexanol molecules to aggregates despite the large enthalpic gain/cost of more than 20 kJ/mol. Calculations were carried out for different concentrations and temperatures using the nonpolarizable TraPPE-UA force field.

The mixtures of 1-hexanol in *n*-hexane considered here are very nonideal, as is evident from an analysis of the radial distribution functions, e.g., the oxygen-oxygen radial distribution function for the 1% solution at  $T = 298$  K shows a first peak with a height of about 850 and a coordination number of about 1.4. Using a stringent set of criteria to determine hydrogen bonding, the distributions over aggregate sizes were calculated. These distributions are bimodal, as is typical for self-aggregating micellar solutions, i.e., they show a large fraction of monomers, few small aggregates (dimers and trimers), an abundance of tetramers and pentamers, and very few larger clusters. About half of the tetramers and pentamers form closed cyclic structures, whereas the other half are linear.

The calculation of equilibrium constant ratios with respect to the formation of dimers points to the importance of cooperativity effects. The equilibrium constant ratios show a strong cluster size dependence with a maximum equilibrium constant ratio for the formation of the tetramer. This is in contrast to the constant equilibrium constant ratio between dimer-like and polymer-like hydrogen bonds postulated by Gupta and Brinkley for their lattice-fluid hydrogen-bonding theory.<sup>9</sup> Ab initio calculations by Sum and Sandler<sup>10</sup> also revealed the size dependence of the equilibrium constant ratios but did not yield any indication of a maximum in this quantity, as would be expected for micellar solutions (compared to a miscibility gap).

Using simulations at different temperatures, the enthalpies of aggregate formation were determined from the temperature dependence of the equilibrium constants. Again, cooperative effects resulted in more favorable enthalpies of aggregate formation for tetramers to hexamers than for dimers and trimers. Comparing the equilibrium constants and the enthalpies of aggregate formation, we can conclude that larger clusters are entropically disfavored compared to the medium-sized tetramers and pentamers. The calculated enthalpies of aggregate formation are about 20% smaller in magnitude than those inferred from NMR experiments for 1-butanol in cyclohexane.<sup>27</sup>

The calculated fractions of free hydroxyl donors (e.g., about 30% for the 3% solution at  $T = 298$  K) are in qualitative, albeit not quantitative, agreement with the experimental results of Gupta and Brinkley.<sup>9</sup> A comparison of the simulation results obtained using two different sets of partial charges for the 1-hexanol headgroup (the TraPPE-UA model representing the induced charges found in neat liquid alcohols and the SM5.4 charges representing an isolated alcohol molecule in an *n*-alkane solution) indicates the need for polarizable force fields to obtain quantitative agreement. The average electrostatic interactions between alcohol molecules would be weakened in a polarizable model compared to the TraPPE-UA model, which would lead to less aggregation, particularly for the lower concentrations. Furthermore, one might expect that a polarizable model would shift the aggregate distribution further toward larger clusters where the induced dipole moments are larger.

**Acknowledgment.** We thank Stan Sandler for encouraging us to start this project; Bin Chen, Pete Carr, and Charles Eckert for many helpful discussions; and Paul Winget for providing the CM2 charges for an isolated 1-hexanol molecule in an *n*-hexane solvent. Financial support from the National Science Foundation (CTS-9813601 and CHE-9816328) and a Sloan Research Fellowship are gratefully acknowledged. Part of the computer resources were provided by the Minnesota Supercomputing Institute.

## References and Notes

- (1) Prausnitz, J. M.; Lichtenthaler, R. M.; de Azevedo, E. G. *Molecular Thermodynamics of Fluid-Phase Equilibria*; Prentice Hall: Englewood Cliffs, NJ, 1986.
- (2) Tanford, C. *The Hydrophobic Effect*; Wiley: New York, 1973.
- (3) Maitland, G. C.; Rigby, M.; Smith, E. B.; Wakeham, W. A. *Intermolecular Forces: Their Origin and Determination*; Clarendon Press: Oxford, U.K., 1987.
- (4) Economou, I. G.; Donohue, M. D. *AIChE J.* **1991**, *37*, 1875.
- (5) Jorgensen, W. L.; Chandrasekhar, J.; Madura, J. D.; Impey, R. W.; Klein, M. L. *J. Chem. Phys.* **1983**, *79*, 926–935.
- (6) Liu, K.; Cruzan, D.; Saykally, R. J. *Science* **1996**, *271*, 929.
- (7) Gregory, J. K.; Clary, D. C.; Liu, K.; Brown, M. G.; Saykally, R. J. *Science* **1997**, *275*, 814.
- (8) Chen, B.; Xing, J.; Siepmann, J. I. *J. Phys. Chem. B* **2000**, *104*, 2391.
- (9) Gupta, R. B.; Brinkley, R. L. *AIChE J.* **1998**, *44*, 207.
- (10) Sum, A. K.; Sandler, S. I. *J. Phys. Chem. A* **2000**, *104*, 1121.
- (11) Martin, M. G.; Siepmann, J. I. *J. Phys. Chem. B* **1998**, *102*, 2569.
- (12) Chen, B.; Potoff, J. J.; Siepmann, J. I. *J. Phys. Chem. B* **2001**, *105*, 3093.
- (13) Jorgensen, W. L.; Madura, J. D.; Swenson, C. J. *J. Am. Chem. Soc.* **1984**, *106*, 6638.
- (14) Jorgensen, W. L. *J. Phys. Chem.* **1986**, *90*, 1276.
- (15) Stubbs, J. M.; Chen, B.; Potoff, J. J.; Siepmann, J. I. *Fluid Phase Equilib.* **2001**, *183/184*, 301.
- (16) Van der Ploeg, P.; Berendsen, A. J. *J. Chem. Phys.* **1978**, *76*, 3271.
- (17) Cornell, W. D.; Cieplak, P.; Bayly, C.; Gould, I. R.; Merz, K. M.; Ferguson, D. M.; Spellmeyer, D. C.; Fox, T.; Caldwell, J. W.; Kollman, P. A. *J. Am. Chem. Soc.* **1995**, *117*, 5179.
- (18) Wood, W. W.; Parker, F. R. *J. Chem. Phys.* **1955**, *27*, 720.
- (19) Allen, M. P.; Tildesley, D. J. *Computer Simulation of Liquids*; Oxford University Press: New York, 1987.
- (20) McDonald, I. R. *Mol. Phys.* **1972**, *23*, 41.
- (21) Siepmann, J. I.; Frenkel, D. *Mol. Phys.* **1992**, *75*, 59.
- (22) Vlucht, T. J. H.; Martin, M. G.; Smit, B.; Siepmann, J. I.; Krishna, R. *Mol. Phys.* **1998**, *94*, 727.
- (23) Martin, M. G.; Siepmann, J. I. *J. Phys. Chem. B* **1999**, *103*, 4508.
- (24) Siepmann, J. I.; McDonald, I. R. *Mol. Phys.* **1992**, *75*, 255.
- (25) Wertz, D. L.; Kruh, R. K. *J. Chem. Phys.* **1967**, *47*, 388.
- (26) Mikusinska-Planner, A. *Acta Crystallogr. A* **1977**, *A33*, 433.
- (27) Karachewski, A. M.; Howell, W. J.; Eckert, C. A. *AIChE J.* **1992**, *37*, 65.
- (28) Schall, H.; Häber, T.; Suhm, M. A. *J. Phys. Chem. A* **2000**, *104*, 265.
- (29) Giesen, D. J.; Storer, J. W.; Cramer, C. J.; Truhlar, D. G. *J. Am. Chem. Soc.* **1995**, *117*, 1057.
- (30) Li, J.; Zhu, T.; Hawkins, G. D.; Winget, P.; Liotard, D. A.; Cramer, C. J.; Truhlar, D. G. *Theor. Chem. Acc.* **1999**, *103*, 9.
- (31) Sear, R. P.; Jackson, G. *J. Chem. Phys.* **1996**, *105*, 1113.
- (32) Guan, B.; Han, B. X.; Yan, H. K. *Fluid Phase Equilib.* **1998**, *149*, 277.
- (33) Stubbs, J. M.; Siepmann, J. I. Unpublished results.
- (34) Chen, B.; Siepmann, J. I. *J. Phys. Chem. B* **2001**, *105* (45), 11275.